MATERIALS SCIENCE

Borophene-graphene heterostructures

Xiaolong Liu[1] and Mark C. Hersam[1,2,3,4]*

Integration of dissimilar two-dimensional (2D) materials is essential for nanoelectronic applications. Compared to vertical stacking, covalent lateral stitching requires bottom-up synthesis, resulting in rare realizations of 2D lateral heterostructures. Because of its polymorphism and diverse bonding geometries, borophene is a promising candidate for 2D heterostructures, although suitable synthesis conditions have not yet been demonstrated. Here, we report lateral and vertical integration of borophene with graphene. Topographic and spatially resolved spectroscopic measurements reveal nearly atomically sharp lateral interfaces despite imperfect crystallographic lattice and symmetry matching. In addition, boron intercalation under graphene results in rotationally commensurate vertical heterostructures. The rich bonding configurations of boron suggest that borophene can be integrated into a diverse range of 2D heterostructures.

INTRODUCTION

Two-dimensional (2D) forms of boron, collectively known as borophene, have attracted significant attention as a distinctive 2D platform in both fundamental and applied contexts (*1*–*3*). For example, borophene is the lightest 2D metal with high in-plane anisotropy that results in unique plasmonic and correlated electron phenomena (*4*, *5*). As a trivalent element, boron has at least 16 allotropes in the bulk (*6*), and similar polymorphism is also observed in the 2D limit, resulting in periodic defect structures that give rise to new borophene phases (*5*). This polymorphism suggests that borophene is an ideal candidate for forming abrupt 2D heterostructures because the diverse bonding configurations of boron should relax crystallographic lattice matching requirements. However, studies of 2D heterostructures involving the family of synthetic 2D materials [e.g., silicene (*7*), stanene (*8*), and germanene (*9*)] have been primarily limited to theoretical modeling due to challenges in finding suitable synthetic conditions.

For conventional 2D materials derived from bulk layered crystals, vertical heterostructures can be realized by mechanical stacking, resulting in many examples in the literature (*10*). On the other hand, 2D lateral heterostructures rely on bottom-up synthesis, leaving a limited number of experimentally realized cases [e.g., MoS_2-WSe_2 (*11*, *12*) and graphene-hBN (*13*)]. Atomically abrupt lateral heterostructure interfaces promise controlled heterojunction functionalities and high-quality edge electrical contacts to 2D materials (*14*). However, because of the covalent bonding in lateral heterostructures, imperfect lattice matching typically results in wide and disordered interfaces. In addition, interfacial alloying reduces the structural and electronic abruptness of lateral heterointerfaces (*15*, *16*). Consequently, it is of high interest to identify 2D materials and corresponding synthetic conditions that yield atomically sharp heterostructures.

Here, we report the integration of borophene into 2D heterostructures with graphene. Despite both crystallographic lattice and symmetry mismatch between borophene and graphene, sequential deposition of carbon and boron on Ag(111) substrates in ultrahigh vacuum (UHV) gives rise to nearly atomically sharp lateral heterointerfaces with preferred lattice alignments, as well as rotationally commensurate vertical heterointerfaces as revealed by UHV scanning tunneling microscopy and spectroscopy (STM/STS). In particular, STM tips functionalized with carbon monoxide (CO) reveal atomically resolved features corresponding to covalent boron-carbon bonds at lateral borophene-graphene heterojunctions. Under the same synthesis conditions, rotationally commensurate vertical borophene-graphene

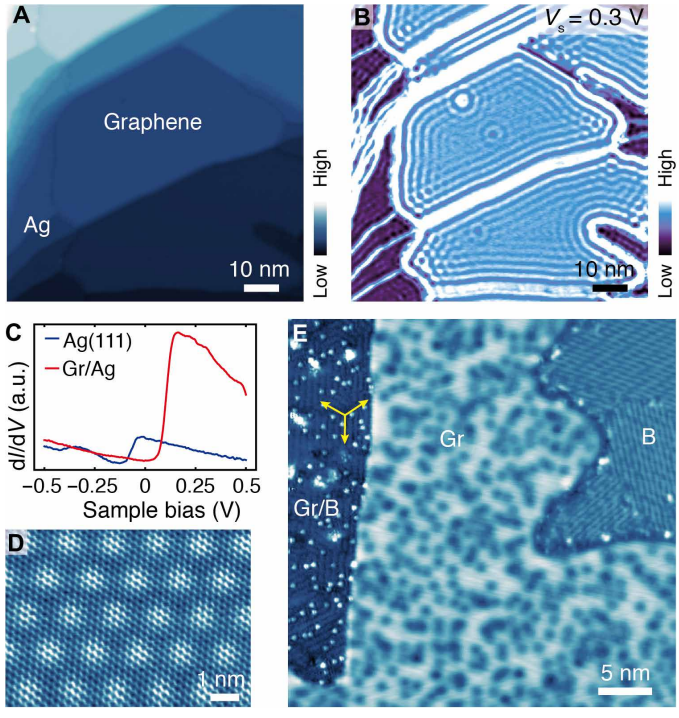

Fig. 1. Graphene and borophene-graphene heterostructures on Ag(111). (**A**) STM topography image of as-grown single-layer graphene on Ag(111) (V_s = 0.3 V, I_t = 500 pA) and (**B**) the corresponding differential tunneling conductance map. (**C**) Differential tunneling conductance curves measured on Ag(111) and graphene (Gr/Ag) with a stabilization condition of V_s = −0.5 V and I_t = 200 pA . (**D**) Atomically resolved STM topography image of as-grown graphene (V_s = 10 mV, I_t = 2 nA). (**E**) STM topography image of lateral and vertical heterostructures between borophene and graphene. Linear features in three directions are indicated by the yellow arrows in the region of borophene-intercalated graphene (Gr/B) (V_s = −5 mV, I_t = 530 pA). a.u., arbitrary units.

[1]Applied Physics Graduate Program, Northwestern University, Evanston, IL 60208, USA. [2]Department of Materials Science and Engineering, Northwestern University, Evanston, IL 60208, USA. [3]Department of Chemistry, Northwestern University, Evanston, IL 60208, USA. [4]Department of Electrical and Computer Engineering, Northwestern University, Evanston, IL 60208, USA.
*Corresponding author. Email: m-hersam@northwestern.edu

heterostructures are also formed by boron intercalation underneath graphene, which electronically decouples graphene from the underlying Ag(111) growth substrate.

RESULTS AND DISCUSSION

The synthesis of borophene-graphene heterostructures begins with submonolayer graphene being grown by electron-beam evaporation of carbon from a graphite rod on a Ag(111) single-crystal substrate held at ~750°C (*17*). Figure 1A shows an STM image of as-grown graphene, where graphene domains are better visualized in dI/dV (Fig. 1B) and |dln$I$/dz| (fig. S1) maps, where I, V, and z are the tunneling current, sample bias, and tip-sample separation, respectively. |dln$I$/dz| is directly related to the apparent tunneling barrier height (ϕ) by $\phi \propto (\mathrm{dln}I/\mathrm{d}z)^2$. The d$I$/d$V$ and |dln$I$/dz| maps reveal a higher local density of states (LDOS) and a lower local work function of graphene, respectively, compared to the Ag(111) substrate. In agreement with previous reports (*18*, *19*), the Ag(111) surface state is manifested as a step feature shifted to positive energies in the dI/dV spectrum of graphene (Fig. 1C), which explains the higher LDOS of graphene in Fig. 1B at 0.3 eV. The high structural quality of single-layer graphene is revealed in Fig. 1D, where both the graphene honeycomb lattice and the Moiré superstructure are evident. Lower temperature growth results in highly dendritic and defective graphene domains (fig. S2). Because of the weak interactions between graphene and the underlying substrate, the rotational alignment of graphene with respect to the underlying Ag(111) is not unique (fig. S3). Borophene is subsequently grown by electron-beam evaporation from a boron rod at a lower substrate temperature (~400° to 500°C). After boron deposition, the STM topography image (Fig. 1E) exhibits neighboring borophene and graphene domains (labeled as B and Gr, respectively), as well as regions within graphene that are later identified as borophene-intercalated graphene (labeled as Gr/B), where linear features oriented in three directions separated by 120° (yellow arrows) are readily visible.

As observed in Fig. 2A (and Fig. 1E), localized dark depressions appear in graphene following boron deposition. To elucidate the origin of these features, a |dln$I$/dz| map of the same area is shown in Fig. 2B, which reveals atomic-sized features associated with topographical depressions. In comparison with the topography image, improved spatial resolution is evident in the |dln$I$/dz| map, particularly in the regions indicated by the white dashed circles due to the increased signal-to-noise ratio achieved with a lock-in amplifier (see the Supplementary Materials for details). Additional improvements in spatial resolution can be achieved by functionalizing the STM tip with CO (*20*) or H_2 (*21*) molecules, which have yielded bond-resolved images in constant-height (CH) (*21*), constant-current (CC) (*22*), dI/dV (*23*), and $\mathrm{d}^2I/\mathrm{d}V^2$ (*24*) images (fig. S4). In particular, LDOS depletion due to Pauli repulsion reduces the tunneling conductance around chemical bonds in CH images (*21*). With a CO-functionalized

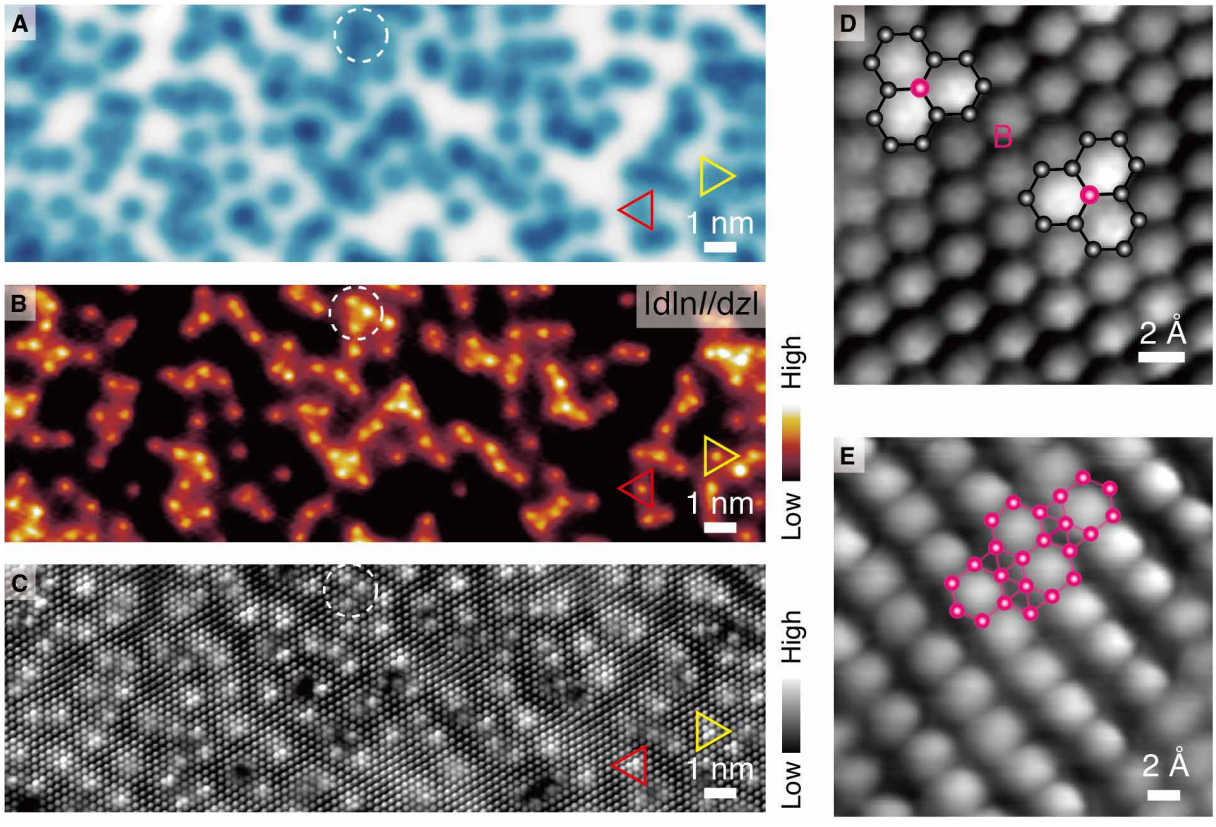

Fig. 2. Substitutional boron doping of graphene. (**A**) STM topography image of single-layer graphene on Ag with a bare metal tip after boron deposition and (**B**) the simultaneously acquired |dln//dz| image (V_s = −4 mV, I_t = 660 pA). The white dashed circles show an example where the |dln//dz| map offers improved spatial resolution. (**C**) Geometric imaging of the same region as in (A) and (B) with a CO-functionalized tip in CH mode (stabilized at V_s = −11 mV, I_t = 80 pA), revealing dopants pointing in opposite directions (red and yellow triangles). (**D**) Substitutional boron dopants in the two sublattices of graphene (stabilized at V_s = −11 mV, I_t = 100 pA). (**E**) Geometric imaging of a $v_{1/5}$ borophene sheet with a CO-functionalized tip in CH mode (stabilized at V_s = −8 mV, I_t = 500 pA).

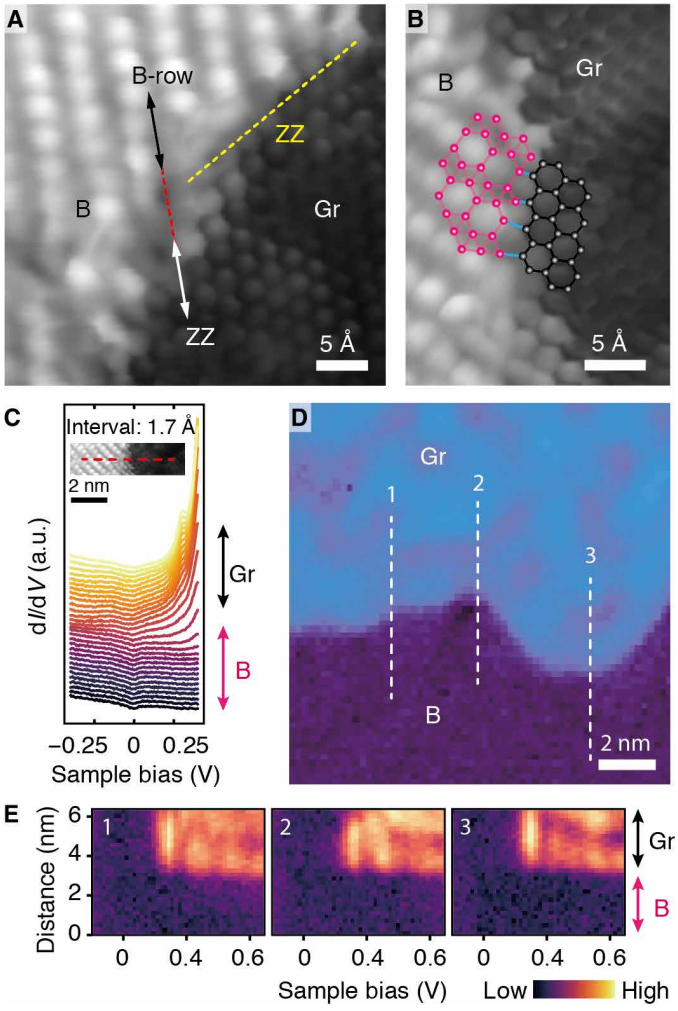

Fig. 3. Borophene-graphene lateral heterostructures. (**A**) Geometric imaging of the borophene-graphene lateral heterointerface with a CO-functionalized tip in CH mode, which resolves both lattices simultaneously (stabilized at $V_s = -10$ mV, $I_t = 350$ pA). The boron row direction is aligned with the graphene ZZ direction as indicated by the black and white double arrows, respectively. (**B**) Zoomed-in image of the heterointerface with a ZZ graphene termination marked by the yellow dashed line in (A) with an overlaid lattice schematic (stabilized at $V_s = -10$ mV, $I_t = 350$ pA). (**C**) Series of STS spectra taken across a lateral heterointerface between borophene and graphene along the red dashed line in the inset with a stabilization condition of $V_s = -0.2$ V, $I_t = 100$ pA. Inset: Stabilized at $V_s = -10$ mV, $I_t = 350$ pA. (**D**) Differential tunneling conductance map (logarithmic scale) of a borophene-graphene lateral heterointerface at $V_s = 0.6$ V (stabilized at $V_s = -0.2$ V, $I_t = 40$ pA). (**E**) Three series of STS spectra taken across three heterointerfaces along the white dashed lines in (D) (stabilized at $V_s = -0.2$ V, $I_t = 40$ pA).

tip, Fig. 2C shows a CH image of the same region as in Fig. 2A, revealing the graphene lattice. Comparing Fig. 2 (A to C), each atomic-sized feature is further resolved as three neighboring bright hexagons pointing in two inequivalent directions. A pair of these features is highlighted by the red and yellow triangles. On the basis of the zoomed-in images (Fig. 2D), these features are in agreement with substitutional boron dopants randomly occupying the two sublattices of graphene (figs. S5 and S6), as indicated by the overlaid structures (*25*). Similarly, CH imaging with a CO-functionalized tip (Fig. 2E) reveals the geometric structure of a $v_{1/5}$ borophene sheet, which was recently observed with CO-functionalized noncontact atomic force microscopy (*26*). The same structure would otherwise be overwhelmed and blurred by electronic features using a bare metal STM tip (fig. S7).

Lateral heterointerfaces between borophene and graphene are expected when borophene grows adjacent to graphene domains with boron substitutional dopants. An example borophene-graphene lateral heterointerface is imaged with a CO-functionalized tip in CH mode in Fig. 3A. To geometrically resolve both lattices simultaneously, imaging at an intermediate tip-sample separation is required (fig. S8). Unlike the lattice-matched and symmetry-matched lateral heterointerfaces of graphene-hBN (*13*) and heterojunctions based on transition metal dichalcogenides (*11*, *12*, *27*), borophene and graphene share minimal structural similarities in terms of lattice constants or crystal symmetry. Despite these crystallographic differences, the borophene-graphene lateral heterointerface in Fig. 3A shows near-atomic sharpness, with the boron row directions aligned with the zigzag (ZZ) directions of graphene. This lattice alignment is preferential for heterointerfaces with both local ZZ and armchair (AC) graphene terminations (figs. S9 and S10). An overlaid atomic structure model is shown in Fig. 3B (zoomed-in image of the ZZ heterointerface is provided in Fig. 3A), where interfacial features corresponding to boron-carbon covalent bonds are marked with blue lines. Because borophene growth is performed at a reduced temperature compared to graphene, the graphene domain edges are unlikely to have high mobility during the formation of the heterointerface with borophene. Therefore, the nearly atomically sharp heterointerface is likely the result of the diverse bonding configurations and multicenter bonding characteristics of boron (*28*). Evidenced from the series of STS spectra in Fig. 3C and the differential tunneling conductance map in Fig. 3D, the electronic transition from graphene to borophene takes place across a distance of ~5 Å with no apparent interface states. In Fig. 3E, the three series of STS spectra taken along the three dashed lines in Fig. 3D confirm that this short-ranged electronic transition is insensitive to local interfacial structures (more spectra and discussion are given in fig. S11 and Supplementary Text, respectively) and comparable to that at borophene-Ag boundaries (fig. S12).

Graphene intercalation [e.g., by Na (*29*)] has been widely explored, although transformations of intercalants into true 2D sheets are relatively rare (*30*). The small atomic radius of boron and weak interaction between graphene and Ag(111) suggest possible intercalation of graphene with boron. Figure 4A provides evidence not only for boron intercalation but also for the formation of borophene-graphene vertical heterostructures, particularly a triangular domain surrounded by graphene. The honeycomb lattice observed on this triangular domain confirms the presence of graphene. However, it exhibits a lower LDOS at −50 meV compared to the surrounding graphene (Fig. 4B). Compared to graphene directly on Ag(111), the lack of a high LDOS feature in the dI/dV spectrum (Fig. 4C, blue curve) corresponding to the Ag(111) surface state is the first piece of evidence suggesting boron intercalation since electronic decoupling of graphene from metal substrates is typically observed after intercalation (*19*). Second, as expected for partial intercalation, the graphene lattice remains continuous across the lateral interface between graphene and the triangular domain (Fig. 4D, which is a zoomed-in image of the red dashed rectangle in Fig. 4A). The CH image of the triangular domain with a CO-functionalized tip (Fig. 4E, which is a zoomed-in image of the yellow dashed rectangle in Fig. 4A) also reveals substitutional boron

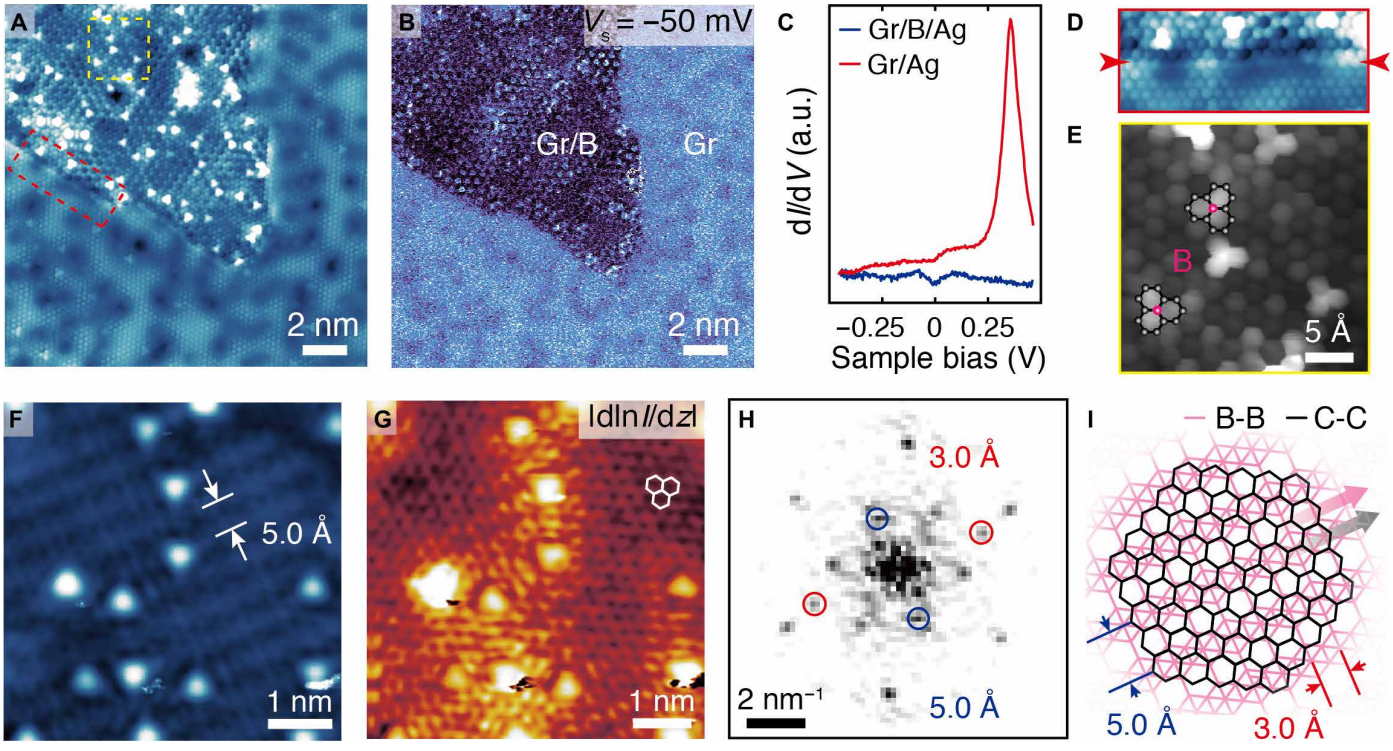

Fig. 4. Borophene-graphene vertical heterostructures. (**A**) STM topography image of a triangular borophene-intercalated graphene domain (V_s = 35 mV, I_t = 250 pA) with a CO-functionalized tip in CC mode and (**B**) differential tunneling conductance map of the same region (V_s = −50 mV, I_t = 200 pA). (**C**) Point STS spectra of graphene and borophene-intercalated graphene (stabilized at V_s = −0.1 V, I_t = 100 pA). (**D**) Zoomed-in STM image of the graphene-graphene/borophene interface (red arrowheads) indicated by the red dashed rectangle in (A) (V_s = 35 mV, I_t = 250 pA). (**E**) Zoomed-in STM image of borophene-intercalated graphene domain indicated by the yellow dashed rectangle in (A) with a CO-functionalized tip in CH mode (stabilized at V_s = 30 mV, I_t = 500 pA). (**F**) STM topography image and (**G**) simultaneously acquired |dln*I*/d*z*| image of borophene-intercalated graphene with a bare metal tip (V_s = −8 mV, I_t = 500 pA). A linear structure with 5 Å periodicity is marked in (F). The graphene lattice is marked in (G). (**H**) Fourier transform of the image in (G), showing an orthogonal pair of points corresponding to a rectangular lattice (3 Å × 5 Å). (**I**) Schematic representation of the rotationally commensurate borophene-graphene vertical heterostructure, where the boron row direction and the graphene AC direction are aligned as indicated by the pink and gray arrows, respectively.

dopants (Fig. 2D). Third, bare metal tips electronically reveal 1D subsurface linear features with a periodicity of 5 Å in the intercalated graphene domains (Fig. 4F and fig. S13), where the graphene lattice is more clearly resolved in the |dln*I*/d*z*| map of the same area (Fig. 4G). These 1D structures resemble the boron rows in the $\nu_{1/6}$ borophene model that are separated by 5 Å (fig. S14). In addition to the set of points corresponding to graphene, the Fourier transform of Fig. 4G displays a pair of orthogonal points corresponding to a 3 Å × 5 Å rectangular lattice (Fig. 4H), which agrees well with the $\nu_{1/6}$ borophene model. Last, the observed threefold lattice orientation of the linear features (Fig. 1E and fig. S14) corresponds well with the same prevailing structure observed for $\nu_{1/6}$ borophene sheets (fig. S14). All of these observations strongly indicate the intercalation of graphene by $\nu_{1/6}$ borophene close to Ag step edges (fig. S15), and thus the formation of borophene-graphene vertical heterostructures, which can be preferentially realized by increasing the initial graphene coverage (fig. S15). On the basis of Fig. 4H, this vertical heterostructure is schematically shown in Fig. 4I, where the boron row direction (pink arrow) is closely aligned with the AC direction of graphene (black arrow), thus forming a rotationally commensurate vertical heterostructure. The ability of borophene to form lateral and vertical heterostructures with graphene suggests a prototypical and generalizable experimental strategy for fabricating synthetic 2D heterostructures with potential utility for nanoelectronic and related technologies.

MATERIALS AND METHODS

Graphene and borophene growth

The growth of graphene and borophene was performed in an UHV preparation chamber with a base pressure of 1×10^{-10} mbar. The Ag(111) single-crystal substrate was cleaned by repeated cycles of Ar^+ sputtering (1×10^{-5} mbar, 800 eV energy, 30 min) and thermal annealing (550°C, 45 min) until an atomically clean and flat Ag(111) surface was obtained. Graphene growth was achieved by electron-beam evaporation (FOCUS EFM3) of a pure graphite rod (diameter, 2.0 mm; purity, 99.997%; Sigma-Aldrich/Goodfellow) onto the heated Ag(111) substrate (~750°C) with a filament current of ~1.6 A and an accelerating voltage of ~2 kV, yielding an emission current of ~70 mA and a carbon flux of ~40 nA. The chamber pressure during graphene growth was ~1×10^{-9} mbar. Subsequently, borophene growth was achieved by electron-beam evaporation (FOCUS EFM3) of a pure boron rod (diameter, 3 to 5 mm; purity, 99.9999%; ESPI Metals) onto heated submonolayer graphene on Ag(111) (400° to 500°C) with a filament current of ~1.5 A and an accelerating voltage of 1.75 kV, yielding an emission current of ~34 mA and a boron flux of ~10 nA. The chamber pressure during borophene growth was ~2×10^{-10} mbar. The flux during the deposition of carbon and boron was measured with built-in flux monitors, which are pairs of biased parallel plates measuring the ion current at the end of the apertures of the evaporators, where the carbon/boron flux exits and travels to

the sample surfaces. To get both lateral and vertical heterostructures, submonolayer graphene coverage of ~50% is preferred and typically used. Higher initial graphene coverage (e.g., ~80%; fig. S15) leaves less uncovered Ag(111) surface for direct borophene growth and thus facilitates the formation of vertical heterostructures and suppresses the growth of lateral heterostructures.

Scanning tunneling microscopy and spectroscopy

UHV STM/STS was performed on a commercial system (Scienta Omicron LT) at ~4 K using electrochemically etched PtIr tips. To functionalize STM tips with CO molecules, the STM chamber was back-filled with pure CO to 1×10^{-5} mbar for 40 s, with the STM shrouds open to allow direct adsorption of CO onto the cold sample surface. Deliberate CO functionalization was achieved by placing the tip on top of an adsorbed CO molecule and ramping the sample bias to −2 mV and tunneling current to ~1 nA. Spontaneous CO functionalization also took place during scanning with low sample biases (<50 mV). STS measurements were performed using a lock-in amplifier (Signal Recovery 7270) with an amplitude of 3 mV_{RMS} and a modulation frequency of 822 Hz. $|d\ln I/dz|$ (where I is the tunneling current and z is the tip-sample separation) measurements were performed with a lock-in amplifier (SRS SR850), where an ac output (863 Hz) voltage was added to the z scanner piezo driving signal, causing a 0.3 Å root mean square (RMS) tip oscillation. SPECS Nanonis electronics and Gwyddion software were used for data acquisition and image processing.

SUPPLEMENTARY MATERIALS

Supplementary material for this article is available at http://advances.sciencemag.org/cgi/content/full/5/10/eaax6444/DC1

Supplementary Text
Fig. S1. |dln//dz| measurements.
Fig. S2. Low-temperature graphene growth.
Fig. S3. Multiple rotational lattice alignments between graphene and Ag(111).
Fig. S4. Comparison of different imaging channels with CO-functionalized tips.
Fig. S5. Random distribution of boron dopants in two sublattices of graphene.
Fig. S6. The absence of hidden Kekulé order.
Fig. S7. Increased spatial resolution enabled by CO functionalization.
Fig. S8. Resolving the geometric structures of borophene and graphene simultaneously.
Fig. S9. Atomically resolved borophene-graphene heterointerfaces with ZZ graphene terminations.
Fig. S10. Atomically resolved borophene-graphene heterointerfaces with AC graphene terminations.
Fig. S11. Electronic transitions across various graphene-borophene heterointerfaces.
Fig. S12. Electronic transitions across graphene-Ag and borophene-Ag interfaces.
Fig. S13. Comparing images taken with bare and CO-functionalized tips.
Fig. S14. Comparing borophene-intercalated graphene with a $v_{1/6}$ borophene sheet.
Fig. S15. Control of heterostructures and distribution of intercalated graphene domains.
References (*31*–*36*)

REFERENCES AND NOTES

1. A. J. Mannix, X.-F. Zhou, B. Kiraly, J. D. Wood, D. Alducin, B. D. Myers, X. Liu, B. L. Fisher, U. Santiago, J. R. Guest, M. J. Yacaman, A. Ponce, A. R. Oganov, M. C. Hersam, N. P. Guisinger, Synthesis of borophenes: Anisotropic, two-dimensional boron polymorphs. *Science* **350**, 1513–1516 (2015).
2. X. Liu, Z. Wei, I. Balla, A. J. Mannix, N. P. Guisinger, E. Luijten, M. C. Hersam, Self-assembly of electronically abrupt borophene/organic lateral heterostructures. *Sci. Adv.* **3**, e1602356 (2017).
3. A. J. Mannix, Z. Zhang, N. P. Guisinger, B. I. Yakobson, M. C. Hersam, Borophene as a prototype for synthetic 2D materials development. *Nat. Nanotechnol.* **13**, 444–450 (2018).
4. Y. Huang, S. N. Shirodkar, B. I. Yakobson, Two-dimensional boron polymorphs for visible range plasmonics: A first-principles exploration. *J. Am. Chem. Soc.* **139**, 17181–17185 (2017).
5. X. Liu, Z. Zhang, L. Wang, B. I. Yakobson, M. C. Hersam, Intermixing and periodic self-assembly of borophene line defects. *Nat. Mater.* **17**, 783–788 (2018).
6. T. Ogitsu, E. Schwegler, G. Galli, β-Rhombohedral boron: At the crossroads of the chemistry of boron and the physics of frustration. *Chem. Rev.* **113**, 3425–3449 (2013).
7. D. Jose, A. Datta, Structures and chemical properties of silicene: Unlike graphene. *Acc. Chem. Res.* **47**, 593–602 (2014).
8. F.-F. Zhu, W.-j. Chen, Y. Xu, C.-l. Gao, D.-d. Guan, C.-h. Liu, D. Qian, S.-C. Zhang, J.-f. Jia, Epitaxial growth of two-dimensional stanene. *Nat. Mater.* **14**, 1020–1025 (2015).
9. M. E. Dávila, L. Xian, S. Cahangirov, A. Rubio, G. Le Lay, Germanene: A novel two-dimensional germanium allotrope akin to graphene and silicene. *New J. Phys.* **16**, 095002 (2014).
10. K. S. Novoselov, A. Mishchenko, A. Carvalho, A. H. Castro Neto, 2D materials and van der Waals heterostructures. *Science* **353**, aac9439 (2016).
11. M.-Y. Li, Y. Shi, C.-C. Cheng, L.-S. Lu, Y.-C. Lin, H.-L. Tang, M.-L. Tsai, C.-W. Chu, K.-H. Wei, J.-H. He, W.-H. Chang, K. Suenaga, L.-J. Li, Epitaxial growth of a monolayer WSe_2-MoS_2 lateral p-n junction with an atomically sharp interface. *Science* **349**, 524–528 (2015).
12. Z. Zhang, P. Chen, X. Duan, K. Zang, J. Luo, X. Duan, Robust epitaxial growth of two-dimensional heterostructures, multiheterostructures, and superlattices. *Science* **357**, 788–792 (2017).
13. L. Liu, J. Park, D. A. Siegel, K. F. McCarty, K. W. Clark, W. Deng, L. Basile, J. C. Idrobo, A.-P. Li, G. Gu, Heteroepitaxial growth of two-dimensional hexagonal boron nitride templated by graphene edges. *Science* **343**, 163–167 (2014).
14. L. Wang, I. Meric, P. Y. Huang, Q. Gao, Y. Gao, H. Tran, T. Taniguchi, K. Watanabe, L. M. Campos, D. A. Muller, J. Guo, P. Kim, J. Hone, K. L. Shepard, C. R. Dean, One-dimensional electrical contact to a two-dimensional material. *Science* **342**, 614–617 (2013).
15. C. Huang, S. Wu, A. M. Sanchez, J. J. P. Peters, R. Beanland, J. S. Ross, P. Rivera, W. Yao, D. H. Cobden, X. Xu, Lateral heterojunctions within monolayer $MoSe_2$-WSe_2 semiconductors. *Nat. Mater.* **13**, 1096–1101 (2014).
16. P. Sutter, R. Cortes, J. Lahiri, E. Sutter, Interface formation in monolayer graphene-boron nitride heterostructures. *Nano Lett.* **12**, 4869–4874 (2012).
17. B. Kiraly, E. V. Iski, A. J. Mannix, B. L. Fisher, M. C. Hersam, N. P. Guisinger, Solid-source growth and atomic-scale characterization of graphene on Ag(111). *Nat. Commun.* **4**, 2804 (2013).
18. W. Jolie, F. Craes, C. Busse, Graphene on weakly interacting metals: Dirac states versus surface states. *Phys. Rev. B* **91**, 115419 (2015).
19. L. Meng, R. Wu, H. Zhou, G. Li, Y. Zhang, L. Li, Y. Wang, H.-J. Gao, Silicon intercalation at the interface of graphene and Ir(111). *Appl. Phys. Lett.* **100**, 083101 (2012).
20. L. Gross, F. Mohn, N. Moll, P. Liljeroth, G. Meyer, The chemical structure of a molecule resolved by atomic force microscopy. *Science* **325**, 1110–1114 (2009).
21. C. Weiss, C. Wagner, C. Kleimann, M. Rohlfing, F. S. Tautz, R. Temirov, Imaging Pauli repulsion in scanning tunneling microscopy. *Phys. Rev. Lett.* **105**, 086103 (2010).
22. R. Temirov, S. Soubatch, O. Neucheva, A. C. Lassise, F. S. Tautz, A novel method achieving ultra-high geometrical resolution in scanning tunnelling microscopy. *New J. Phys.* **10**, 053012 (2008).
23. O. Krejčí, P. Hapala, M. Ondracek, P. Jelínek, Principles and simulations of high-resolution STM imaging with a flexible tip apex. *Phys. Rev. B* **95**, 045407 (2017).
24. C.-l. Chiang, C. Xu, Z. Han, W. Ho, Real-space imaging of molecular structure and chemical bonding by single-molecule inelastic tunneling probe. *Science* **344**, 885–888 (2014).
25. R. R. Cloke, T. Marangoni, G. D. Nguyen, T. Joshi, D. J. Rizzo, C. Bronner, T. Cao, S. G. Louie, M. F. Crommie, F. R. Fischer, Site-specific substitutional boron doping of semiconducting armchair graphene nanoribbons. *J. Am. Chem. Soc.* **137**, 8872–8875 (2015).
26. X. Liu, L. Wang, S. Li, M. S. Rahn, B. I. Yakobson, M. C. Hersam, Geometric imaging of borophene polymorphs with functionalized probes. *Nat. Commun.* **10**, 1642 (2019).
27. S. Xie, L. Tu, Y. Han, L. Huang, K. Kang, K. U. Lao, P. Poddar, C. Park, D. A. Muller, R. A. DiStasio Jr., J. Park, Coherent, atomically thin transition-metal dichalcogenide superlattices with engineered strain. *Science* **359**, 1131–1136 (2018).
28. I. A. Popov, A. I. Boldyrev, Classical and multicenter bonding in boron: Two faces of boron, in *Boron*, D. Hnyk, M. McKee, Eds. (Springer, 2015), vol. 20 of *Challenges and Advances in Computational Chemistry and Physics*.
29. A. Sandin, T. Jayasekera, J. E. Rowe, K. W. Kim, M. B. Nardelli, D. B. Dougherty, Multiple coexisting intercalation structures of sodium in epitaxial graphene-SiC interfaces. *Phys. Rev. B* **85**, 125410 (2012).
30. Z. Y. Al Balushi, K. Wang, R. K. Ghosh, R. A. Vilá, S. M. Eichfeld, J. D. Caldwell, X. Qin, Y.-C. Lin, P. A. DeSario, G. Stone, S. Subramanian, D. F. Paul, R. M. Wallace, S. Datta, J. M. Redwing, J. A. Robinson, Two-dimensional gallium nitride realized via graphene encapsulation. *Nat. Mater.* **15**, 1166–1171 (2016).
31. J. Tian, H. Cao, W. Wu, Q. Yu, Y. P. Chen, Direct imaging of graphene edges: Atomic structure and electronic scattering. *Nano Lett.* **11**, 3663–3668 (2011).
32. S. Heidorn, K. Morgenstern, Spatial variation of the surface state onset close to three types of surface steps on Ag(111) studied by scanning tunneling spectroscopy. *New J. Phys.* **13**, 033034 (2011).

33. E. Mariani, L. I. Glazman, A. Kamenev, F. von Oppen, Zero-bias anomaly in the tunneling density of states of graphene. *Phys. Rev. B* **76**, 165402 (2007).
34. F. Craes, S. Runte, J. Klinkhammer, M. Kralj, T. Michely, C. Busse, Mapping image potential states on graphene quantum dots. *Phys. Rev. Lett.* **111**, 056804 (2013).
35. G. Giovannetti, P. A. Khomyakov, G. Brocks, V. M. Karpan, J. van den Brink, P. J. Kelly, Doping graphene with metal contacts. *Phys. Rev. Lett.* **101**, 026803 (2008).
36. C. Gutiérrez, C.-J. Kim, L. Brown, T. Schiros, D. Nordlund, E. B. Lochocki, K. M. Shen, J. Park, A. N. Pasupathy, Imaging chiral symmetry breaking from Kekulé bond order in graphene. *Nat. Phys.* **12**, 950–958 (2016).

Acknowledgments
Funding: This work was supported by the Office of Naval Research (ONR N00014-17-1-2993) and the NSF Materials Research Science and Engineering Center (NSF DMR-1720139). X.L. further acknowledges support from a Ryan Fellowship that is administered through the Northwestern University International Institute for Nanotechnology. **Author contributions:** X.L. and M.C.H. conceived the experiments. X.L. performed sample preparation, STM/STS characterization, and data analysis. Both authors contributed to data interpretation and manuscript writing. **Competing interests:** The authors declare that they have no competing interests. **Data and materials availability:** All data needed to evaluate the conclusions in the paper are present in the paper and/or the Supplementary Materials. Additional data related to this paper may be requested from the authors.

Submitted 10 April 2019
Accepted 17 September 2019
Published 11 October 2019
10.1126/sciadv.aax6444

Citation: X. Liu, M. C. Hersam, Borophene-graphene heterostructures. *Sci. Adv.* **5**, eaax6444 (2019).

Borophene-graphene heterostructures

Xiaolong Liu and Mark C. Hersam

Sci Adv **5** (10), eaax6444.
DOI: 10.1126/sciadv.aax6444